

## From automata to fluid flow: Comparisons of simulation and theory

Leo P. Kadanoff, Guy R. McNamara, and Gianluigi Zanetti\*

*The Research Institutes, The University of Chicago, 5640 South Ellis Avenue, Chicago, Illinois 60637*

(Received 16 March 1988; revised manuscript received 18 April 1989)

Lattice-gas automata have been proposed as a new way of doing numerical calculations for hydrodynamic systems. Here, a lattice-gas simulation is run to see whether its behavior really does correspond, as proposed, to that of the Navier-Stokes equation. The geometry used is the two-dimensional version of laminar pipe flow. Three checks on the existing theory are performed. The parabolic profile of momentum density arising from the dynamics is quantitatively verified. So is the equation of state, which arises from the statistical mechanics of the system. Finally, the well-known logarithmic divergence in the viscosity is observed in the automaton and is shown to disagree with the earliest theoretical predictions in this system. Proper agreement is achieved, however, when the theory is extended to include three extra (recently discovered) conserved quantities. In this way, checks of both linear and nonlinear parts of the hydrodynamic description of lattice-gas automata have been achieved.

### I. INTRODUCTION

Recently, Frisch, Hasslacher, and Pomeau<sup>1</sup> have proposed a novel technique, the lattice-gas automation (LGA), for the numerical solution of the incompressible Navier-Stokes equation in two dimensions (2D). This technique has been extensively applied in numerical simulations and it has been extended to schemes for the simulation of 3D incompressible Navier-Stokes flows,<sup>2</sup> binary fluids,<sup>3</sup> buoyant fluids,<sup>4</sup> and other related problems.<sup>5,6</sup>

The idea in Ref. 1 is to mimic a two-dimensional gas with a collection of particles that can move along the edges of a regular lattice in such a way that they are on its sites at integer times. There is only a finite number of velocities; collisions between particles can happen only on the sites of the lattice, and these collisions can be set up to satisfy local conservation laws of mass and linear momentum. Macroscopic fields (e.g., number and momentum density) can be obtained by a coarse-grained averaging in space and time of the corresponding microscopic quantities. The fictitious world of the LGA and the dynamics of its inhabitants are rather arbitrary. Previous workers<sup>1,7,8</sup> have argued that in the long-wavelength limit the conservation laws completely dominate the description of the lattice-gas automata. Hence, they argue, the LGA should have hydrodynamic behavior. The derivation of the hydrodynamic description of the lattice gas is based on general many-body physics arguments and it seems rather convincing. The hydrodynamics of the LGA is described in terms of conserved quantities. These are divided into two classes. The first were imposed on the model, i.e., mass and momentum; the second are the conserved quantities that correspond to extensive invariants peculiar to the LGA model. The second class of conserved quantities was discovered only recently. They are the analog of the phenomenon of fermion doubling well known in lattice gauge theory. They

are discussed in some detail in Refs. 9 and 10; however, the presence of these new invariants can be easily understood by using a trivial one-dimensional example. Let  $g(x)$  be the linear momentum of the particles present at site  $x$ , define

$$G_e(t) = \sum_{x \text{ even}} g(x,t), \quad G_o(t) = \sum_{x \text{ odd}} g(x,t)$$

as the total momentum of the particles on even or odd sites, and let the collision rules conserve the momentum and the number of particles at each site. Since the particles can only hop between nearest neighbors,  $G_e$  and  $G_o$  are exchanged at each time step. The dynamics of this one-dimensional model allow three conserved quantities:  $M$ ,  $G_e + G_o$ , and  $H = (-1)^x(G_e - G_o)$ . The first two are the usual total number of particles and the total linear momentum; the third is due to our extremely simplified dynamics. The staggered momentum  $H$  and its related density  $h$  can be easily generalized to the two- and three-dimensional models currently used, since they are all based on local collision rules and a finite number of velocities. In particular, for the two-dimensional model introduced in Ref. 8 there are three independent conserved densities,  $h_\alpha$ ,  $\alpha = 1, 2, 3$  (one for each symmetry axis of the hexagonal cell), that are the analogs of the staggered momentum density described above.

The hydrodynamic behavior of the two-dimensional LGA is therefore described by six hydrodynamic variables, i.e., the number density, the two components of momentum density, and the three staggered momentum densities. The staggered momentum density and the momentum density are nonlinearly coupled. However, if the staggered momentum densities could be neglected (i.e., put to zero), the resulting equations for the momentum and number densities would then be qualitatively similar to the equations controlling a simple two-dimensional fluid, and it would be possible to regain the

Navier-Stokes equation in the incompressible limit by an opportune redefinition of the units of momentum density and time.

While the  $h_\alpha$  appear in the expression for the momentum current as a source term, the staggered momentum densities are merely convected by the momentum density and there is no mechanism, at the order at which the equations have been derived, for the self-generation of  $h$ . Thus, if the staggered momentum densities are not present in the simulation initial conditions, i.e., if the initial condition's projections on the  $h$  modes are negligible, it should be possible to use the LGA for the numerical solution of the Navier-Stokes equation. This seems consistent with the many simulation results previously reported, which, with the exception of a purposely constructed pathological case, do not seem to be affected by the staggered momentum density. (See, however, Appendix D.)

The purpose of this paper is to check the hydrodynamic behavior of the lattice-gas automaton. Quantitative and semiquantitative tests of the lattice-gas automaton properties have already been reported by various authors.<sup>11-14</sup> The tests we describe in this paper are at least one order of magnitude more accurate than those previously presented. They probe a gross and a rather delicate feature of the system. The gross feature is the parabolic momentum density profile expected in pipe (or Poiseuille) flow. The more delicate feature is the famous<sup>15-18</sup> long-wavelength divergence of the transport coefficients of simple two-dimensional fluids. By comparing the simulation results with the analogous theoretical prediction, we obtain an incisive and significant test of both the gross and the delicate aspects of the lattice-gas automaton hydrodynamic description.

The flow we actually simulated, even though it gives parabolic momentum density profiles, is not a standard channel flow; rather than using traditional<sup>12,14,19</sup> (i.e., no slip) boundary conditions on the channel walls parallel to the flow, we doubled the channel width, set up periodic boundary conditions in both directions, and forced the LGA fluid along opposite directions in the two halves (see Sec. II B 1 and Fig. 1). The resulting flow avoids corrections to the momentum density profile due to wall effects (of the order of the ratio between the particle mean free path and the width of the channel). Instead, the major corrections expected are exponentially small (of order  $\exp[-(\text{channel width})/(\text{mean free path})]$ ). This approach permits us to use the simulations as a precise viscometer even for small channel widths.

We chose this simulation geometry because of its simplicity and because the resulting flow, at the level of forcing we used, is steady and thus allows the construction of local equilibrium densities by time averaging. It should be mentioned, however, that the simulation results that we report here were obtained before one of us (G.M.) discovered the staggered momentum densities, and thus the amplitudes of the staggered momentum modes were not monitored. We will argue in Appendix D, however, that in our simulation, the  $h_\alpha$  densities can give corrections of order  $1/(\text{volume})$  to the quantities we measure, corrections that can be safely neglected. These correc-

tions may, in fact, be the dominant errors in the calculation.

The local equilibrium momentum density profiles obtained from the simulations agree very well (Fig. 4) with the momentum density profile predicted by the long-wavelength expression for the conservation laws derived in Ref. 1 and the assumption of negligible  $h_\alpha$ .

The simulation scheme described above provides us with a precise viscometer. It is true that it measures a transport coefficient in a stressed medium,<sup>20,21</sup> instead of the true equilibrium kinematic viscosity  $\nu$ , but the correction to  $\nu$  due to the applied stress appears to be negligible at the level of forcing used (see Sec. III B 1). Moreover, in contrast to the other direct measurement techniques attempted thus far, namely, transverse wave relaxation<sup>22</sup> and direct measurement of the Green-Kubo autocorrelation function,<sup>23</sup> our method allows measurements of kinematic viscosity averaged over very long times (many turnover times,  $\approx L^2/\nu$ , of the largest eddy in the system). Thus there is enough time to build up hydrodynamic contributions to  $\nu$  and hence permit us to study this delicate feature of the system.

To get the theory for this effect, we recall that the bare transport coefficients of a simple fluid are renormalized by corrections whose origin is essentially hydrodynamic. By using standard mode-mode coupling or other equivalent techniques,<sup>17,24,25</sup> it is possible to estimate, in first-order perturbation theory, the structure and the amplitude of this correction in terms of bare transport coefficients and some thermodynamic derivatives. The result of the calculation is logarithmically divergent in the long-wavelength limit for two dimensions. If we assume that the dynamic of the LGA fluid fluctuations is controlled by the macroscopic conservation laws [Eqs. (1)-(4) of Sec. II], then the same calculation applies to the lattice-gas automaton and gives a quantitative estimate for the amplitude of the logarithmic correction. Note that this amplitude is a sum of contributions corresponding to the nonlinear term present in the momentum density current. Thus it includes contributions due to the staggered momentum densities that would not be present in the equivalent calculation for a simple two-dimensional fluid. We now summarize our results and conclude this section with an outline of the body of the paper.

There is no evident discrepancy between the macroscopic (long-wavelength) description of the lattice-gas automaton given in Ref. 1 and the simulation data: our results indicate that this fluid is able to reproduce parabolic momentum density profiles in the simulation of a uniformly forced channel flow with an accuracy better than 1%. We also have direct evidence that the kinematic viscosity depends indeed on the width of the simulation channel and that this dependence is quantitatively consistent with the logarithmic prediction of the mode-mode coupling calculation. Our simulations studied the largest range of channel width, from 10 to 70 typical mean free paths, that we thought was compatible with our computer resources. For each viscosity measurement point, we performed several runs so that we could quote error bars with reasonable confidence.

According to theory, the nonlinear coupling between momentum and staggered momentum densities clearly makes a 30% contribution to the amplitude of the renormalization. The agreement between the calculated and observed viscosities then demonstrates the necessity for the inclusion of this effect in a correct description of the system.

This paper does not make any claims about the relative efficiency<sup>26</sup> of this simulation technique versus the other more standard ways to solve the incompressible Navier-Stokes equation, and neither do we claim to have explored in detail how the  $h$  modes affect the macroscopic flow of the LGA. We are only concerned with studying the hydrodynamic properties of the lattice-gas automaton in a very simple situation.

The paper is organized as follows. Section II is dedicated to the setting up of the channel-flow simulation together with a brief introduction to the LGA. The main results presented in this section are the parabolic momentum density profile (Fig. 4) and the check of the equation of state for the gas (Fig. 6).

The first part of Sec. III outlines the mode-mode coupling calculation (the actual calculation is done in Appendix A), while Sec. III B discusses how the measured viscosity depends on the parameters of the simulation, i.e., average particle density, system size, and forcing level. Once again, the main result, the comparison between the simulation data and the mode-mode coupling prediction, is a graph (Fig. 10). Section IV of the paper summarizes our conclusions. Appendix B is dedicated to the discussion of the linear stability of the channel flow; Appendix C gives some estimates for the statistical errors in the measurement of the kinematic viscosity, while in Appendix D we estimate the influence of the staggered momentum densities on our simulations.

## II. CHANNEL FLOW

### A. The lattice gas

In this section, we examine the hydrodynamic behavior of the LGA fluid by simulating a forced two-dimensional channel flow. We start with a brief introduction to the lattice gas, intended to fix the notation used in the rest of the paper. The reader will find a more complete description in Ref. 8.

The LGA used in the simulations admits seven different “flavors” of particles, each type being defined by its velocity.<sup>22</sup> There are six velocities parallel to the nearest-neighbor lattice directions with a magnitude of one lattice spacing  $a$  per time step. (See Fig. 1.) The seventh type is a stationary particle with velocity zero. Hence the seven velocities are  $\{\hat{C}_\alpha; \alpha=0, \dots, 6\}$ , with

$$C_0=0,$$

$$C_\alpha = a(\cos[\pi(\alpha-1)/3], \sin[\pi(\alpha-1)/3]), \quad \alpha=1, \dots, 6$$

where we have chosen to orient the lattice as shown in Fig. 1. At each site  $\mathbf{r}$  (we use  $\mathbf{r}$  to label the sites of the lattice) we allow no more than one particle with velocity  $C_\alpha$ , and we indicate with the Boolean vector  $\{f_\alpha(\mathbf{r})\}$  the

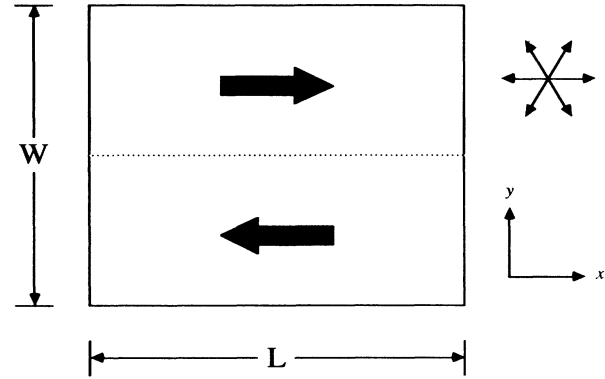


FIG. 1. The simulation model. Periodic boundary conditions are employed in both  $x$  and  $y$  directions. The dotted line indicates the separation of the system into two channels. A uniform body force induces fluid flow in each channel in the direction indicated by the solid arrows. The representative lattice site shown in the upper right-hand corner illustrates the orientation of the underlying hexagonal lattice.

presence  $[f_\alpha(\mathbf{r})=1]$  or the absence  $[f_\alpha(\mathbf{r})=0]$  of a particle with velocity  $C_\alpha$  at site  $\mathbf{r}$ .

With each site we can now associate the microscopic number density,  $n(\mathbf{r}) = \sum_\alpha f_\alpha(\mathbf{r})$ , and the microscopic momentum density,  $g_i(\mathbf{r}) = \sum_\alpha C_{\alpha,i} f_\alpha(\mathbf{r})$  (we formally assume that each particle has unit mass). From here onward we reserve the latin indices for the Cartesian coordinates, and summation on repeated indices is understood.

The time evolution of the system is expressed as the composition of two steps: in the “streaming” step, each particle hops from its current site to the next-neighbor site lying in the direction of its velocity. In the “collision” step, the particles at each site are redistributed among the seven velocities in such a way that, site by site, the number of particles and the momentum is conserved.

To achieve this, we follow previous workers<sup>27,22</sup> and divide the  $2^7$  possible configurations at a site into classes. Each class contains configurations with the same total momentum  $\mathbf{g}$  and number of particles  $n$ . The nontrivial classes are those containing more than one element. The ones involving two or three particles are shown in Fig. 2. Note that these classes all have either two or three elements. Since the collision rules are invariant under hole-particle interchange, it is sufficient to show only the two- and three-particle nontrivial configuration classes. During the collision step, wherever a lattice site falls into one of these nontrivial classes, a collision occurs and the configuration changes to another element of the same class. In cases where there are two possible choices for the collision output [such as the class  $(n=2, \mathbf{g}=0)$  of Fig. 2], we use the parity of the time step to determine the outcome, rather than use a random number generator. Thus we avoid chirality but the model remains fully deterministic.

The total number of particles and the total momentum are obviously conserved by the dynamic of the model. A

n	g	s	Particle Configurations
2	0	6	
2	1	24	
3	0	4	
3	0	6	
3	1	36	

FIG. 2. We have divided the possible configuration of particles at a site into classes. In a collision, the input particle configuration is changed into another element of the same class. For each class we list  $n$ , the total number of particles present at the site,  $g$  the modules of the total momentum, and  $s$  the number of possible configurations that can be constructed from the given class using the particle-hole symmetry and the hexagonal symmetry. The classes with only one element (i.e., no collision is possible) are not listed. All the other possible configurations can be constructed by using the particle-hole symmetry and the hexagonal symmetry.

less obvious extensive invariant is the total staggered momentum

$$H_\alpha = (-1)^t \sum_{\mathbf{r} \in \Omega} (-1)^{\mathbf{B}_\alpha \cdot \mathbf{r}} \mathbf{C}_\alpha^\perp \cdot \mathbf{g}(\mathbf{r}, t),$$

where  $\mathbf{C}_\alpha^\perp$  is obtained by rotating  $\mathbf{C}_\alpha$  by  $\pi/2$  counterclockwise, and  $\mathbf{B}_\alpha$  is the reciprocal space vector perpendicular to  $\mathbf{C}_\alpha$ , i.e.,  $\mathbf{B}_\alpha = (2/\sqrt{3})\mathbf{C}_\alpha^\perp$ . The corresponding density is

$$\begin{aligned} \bar{\Pi}_{mi}(\mathbf{r}, t) = & \delta_{mi} p(\mathbf{r}, t) + \lambda \left[ \bar{g}_m(\mathbf{r}, t) \bar{g}_i(\mathbf{r}, t) + \sum_{\alpha=1}^3 C_{\alpha,m}^\perp C_{\alpha,i}^\perp \bar{h}_\alpha(\mathbf{r}, t) \bar{h}_\alpha(\mathbf{r}, t) \right] \\ & + \nu [\partial_{x_j} \bar{g}_m(\mathbf{r}, t) + \partial_{x_m} \bar{g}_j(\mathbf{r}, t)] + (\zeta - \nu) \delta_{mi} \partial_{x_k} \bar{g}_k(\mathbf{r}, t), \end{aligned} \quad (2a)$$

and the staggered momentum currents are

$$\begin{aligned} \bar{J}_{\alpha,m}(\mathbf{r}, t) = & \frac{\lambda}{2} (\delta_{mj} + 2C_{\alpha,m}^\perp c_{\alpha,j}^\perp) \bar{g}_j(\mathbf{r}, t) \bar{h}_\alpha(\mathbf{r}, t) \\ & + (\kappa_1 \delta_{mi} + \kappa_2 C_{\alpha,m}^\perp C_{\alpha,i}^\perp) \partial_{x_i} \bar{h}_\alpha(\mathbf{r}, t). \end{aligned} \quad (2b)$$

The coefficient of the ‘‘convective’’ term is given explicitly by

$$h_\alpha(\mathbf{r}, t) = (-1)^t (-1)^{\mathbf{B}_\alpha \cdot \mathbf{r}} \mathbf{C}_\alpha^\perp \cdot \mathbf{g}(\mathbf{r}, t).$$

The index  $\alpha$  in  $H_\alpha$  runs over  $\{1, \dots, 6\}$ , but  $H_{\alpha+3} = -H_\alpha$  and thus it is sufficient to choose  $\alpha = 1, 2, 3$ . The total staggered momentum densities are invariant for the case of periodic boundary conditions with an even number of lattice rows and columns.<sup>9</sup>

The lattice automaton fluid is expected to have hydrodynamic behavior in the long-wavelength limit, and the microscopic conservation laws become

$$\begin{aligned} \partial_t \bar{n} + \partial_k \bar{g}_k &= 0, \\ \partial_t \bar{g}_i + \partial_k \bar{\Pi}_{ik} &= 0, \\ \partial_t \bar{h}_\alpha + \partial_k \bar{J}_{\alpha k} &= 0, \end{aligned} \quad (1)$$

where  $\bar{n}$ ,  $\bar{g}_i$ , and  $\bar{h}_\alpha$  are the macroscopic densities, while  $\bar{g}_k$ ,  $\bar{\Pi}_{ik}$ , and  $\bar{J}_{\alpha k}$  are the respective currents obtained from their microscopic counterparts by a suitable coarse-grained averaging procedure.

The macroscopic densities are assumed to be small, slowly varying perturbations of the thermodynamic equilibrium state which has zero average momentum and staggered momentum densities and an average number density equal to  $7d$ . The reduced density  $d$  ( $0 \leq d \leq 1$ ) is the corresponding average number of particles per link. Equation (1) is considered true in the long-wavelength limit, and thus  $\mathbf{r}$  and  $t$  are treated as continuous variables in that expression.

Equation (1) makes a statement concerning the existence of conservation laws for the macroscopic densities of the lattice-gas automaton. To be useful, it must be augmented by a constitutive relation for the stress tensor  $\bar{\Pi}_{ik}$  and the staggered momentum current  $\bar{J}_{\alpha k}$ . The crucial physical assumption is that the LGA will respond to perturbations by quickly reaching a state for which the hypotheses of local equilibrium are valid, and in which there are linear relations between the dissipative fluxes of the conserved densities and their gradients. These constitutive relations and Eq. (1) provide a closed set of partial differential equations for the local equilibrium fields  $\bar{n}$ ,  $\bar{g}$ , and  $\bar{h}$ . The current  $\bar{\Pi}_{mi}(\mathbf{r}, t)$  is given by

$$\lambda = \frac{1-2d}{12d(1-d)}, \quad (3)$$

and the ‘‘pressure’’  $p$  is given to second order in  $\bar{g}$  and  $\bar{h}$  by

$$\begin{aligned} p(\mathbf{r}, t) = & c^2 \bar{n}(\mathbf{r}, t) - \lambda c^2 \left( \frac{\zeta}{6} \right) [\bar{g}_m(\mathbf{r}, t) \bar{g}_m(\mathbf{r}, t) \\ & + \bar{h}_\alpha(\mathbf{r}, t) \bar{h}_\alpha(\mathbf{r}, t)]. \end{aligned} \quad (4)$$

The quantities  $\nu$ ,  $\zeta$ ,  $\kappa_1$ , and  $\kappa_2$  can be identified as transport coefficients, while  $c$  is the speed of sound for the gas. We call  $\nu$  the kinematic viscosity and  $\zeta$  the bulk viscosity. The staggered momentum transport coefficients  $\kappa_1$  and  $\kappa_2$  do not have an analog in simple fluids. In the seven-velocity model used in the simulations  $c = \sqrt{3/7}$ .

The first two terms of the right-hand side of Eq. (2a), the Eulerian part of  $\bar{\Pi}_{ij}$ , are obtained from the local equilibrium approximation of the gas. They are the leading contributions in the Taylor-series expansion of the equilibrium stress tensor in powers of the equilibrium average momentum density and staggered momentum density. The dissipative part of Eq. (2a) can be easily found using standard techniques.<sup>8,10</sup> In writing it we neglected the remainder, fourth order in  $\bar{g}, \bar{h}$ , of the Taylor-series expansion and, as usual in the long-wavelength limit, higher-order derivatives. The constitutive expression for the  $h$  current has been obtained in an analogous way.

The physical processes described in Eq. (2b), the constitutive equation for the  $\bar{h}$  current, are convection [by the  $\bar{g}_i(vr, t)$ ] and diffusion, but neither of the corresponding terms in Eq. (2b) has rotational symmetry. This should not be surprising since the staggered momentum modes are very strongly tied to the microscopic structure of the model.

The constitutive equation presented in Eq. (2a) show some unexpected and striking features. In fact, Eq. (2a) contains, together with a pressure term and a “standard” momentum convection term, a term that depends only on the  $\bar{h}_\alpha(\mathbf{r}, t)$  densities. This term (together with a similar one concealed in the definition of  $p$ ) makes the macroscopic behavior of the LGA fundamentally different from that of simple real fluids. In fact, the  $h$  modes can act as a source, through the pressure term and/or the other term explicitly indicated in Eq. (2a) for the  $\bar{g}_m$  density. Hence the LGA can produce flows that are not solutions of the Navier-Stokes equation. However, there is no production mechanism for  $h_\alpha$  in Eq. (2b). Thus, unless  $h_\alpha$  is injected in the initial conditions of the simulation, the flow resulting from the simulation should be well described by the number and momentum density alone. This seems to be the case for the simulation results reported in the literature (see Ref. 10, however, for a pathological case) and for our channel flow (see Appendix D).

The coefficient  $\lambda$  multiplies all the nonlinear terms present in Eqs. (2a) and (2b). For the purpose of this paper, cf. Sec. III, the dependence of  $\lambda$  in  $d$ , Eq. (3), has a useful application. In fact, for  $d = \frac{1}{2}$ ,  $\lambda$  is zero. We will exploit this fact, easily explained by the particle-hole symmetry of the gas,<sup>28</sup> as a useful check for the results of Secs. III A and III B.

## B. Channel simulations

### 1. Simulation setup

The simulation system we have employed is a model of forced 2D Poiseuille flow.<sup>4,6,12,14</sup> The system is a hexagonal lattice with an equal number of rows and columns and periodic boundary conditions in both the horizontal and vertical directions (Fig. 1). Note that the system

width  $W$  is  $\sqrt{3}/2$  times the length  $L$  due to the unequal row and column spacings. We divide the system into two horizontal channels, as indicated by the dotted line in Fig. 1. Fluid flow is established in the two channels by injecting momentum in the  $+x$  direction in the upper channel, and in the  $-x$  direction in the lower channel. This momentum is injected uniformly across the width and length of each channel in the following fashion. After each time step we randomly select a lattice site and, if possible, apply one of the microscopic forcing rules described in Fig. 3. Each successful application of a forcing rule adds one unit of momentum to the system. The forcing process is repeated until the desired amount of momentum has been transferred to the gas; fractional amounts of momentum to be added to the system are accumulated across time steps until they sum to an amount greater than 1, at which time one additional unit of momentum is added to the gas. The same number of forcing operations is performed in each channel; consequently, the total  $x$  momentum in the system remains constant at its initial value of 0 (the total  $y$  momentum is also initialized to 0). The result of this process is a constant body force applied to the gas uniformly across the width and length of each channel, but acting in opposite directions in the two halves of the system.<sup>29</sup>

The forcing level employed in the present work varies from 0.2 to 0.5 units of momentum applied to each channel per time step. Within this range, the resulting flow is

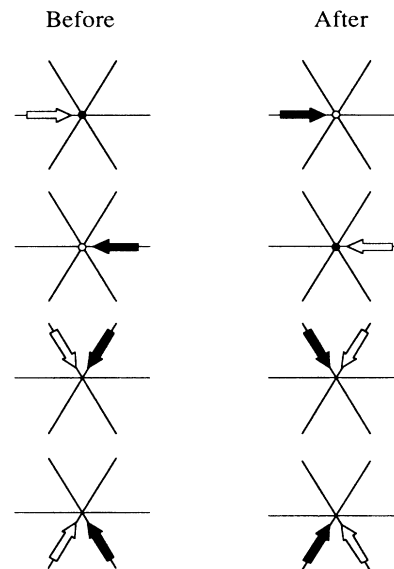


FIG. 3. Forcing rules. The four pairs of diagrams represent the four microscopic forcing rules used to inject momentum into the upper channel. The shaded symbols represent particles while the outlined symbols represent holes. Each transformation adds to the fluid one unit of momentum in the plus  $x$  direction. A similar set of forcing rules, obtained by reflecting the individual diagrams about the  $y$  axis, is used in the lower channel to inject momentum in the minus  $x$  direction.

steady when averaged over a period of the order of a few dissipation times,  $\approx L^2/\nu$ . For a steady flow, the equations for the forced flow<sup>4,8</sup> become

$$\begin{aligned} \partial_k \bar{g}_k &= 0, \\ \partial_k (\lambda \bar{g}_k \bar{g}_l) &= -\partial_l p + \partial_k (\nu \partial_k \bar{g}_l) + \bar{f}_l, \end{aligned} \quad (5)$$

where  $\bar{f}$  is the average force per site. The combination of a uniform body force aligned with the  $x$  direction and the assumption of vanishing fluid velocity along the channel boundaries gives rise [through Eq. (5)] to a parabolic momentum density profile in each channel:

$$\bar{g}_x(y) = \frac{\bar{g}_{\max}}{(W/4)^2} [(W/4)^2 - y^2], \quad (6)$$

with  $\bar{g}_y = 0$  and

$$\bar{g}_{\max} = \frac{\sqrt{3}WF}{32L\nu}, \quad (7)$$

where  $F$  is the total force applied to the channel (notice that with the definitions we use  $L^2$  is equal to  $N$ , the number of sites in the system),  $y$  is measured from the center of the channel, and we have neglected the corrections  $O(\bar{g}_x(\partial_y \bar{g}_x)^2)$  due to variation of  $\bar{n}$  across the width of the channel. We extract this momentum profile from the simulation by averaging the microscopic momentum density in time and along the lattice rows (lines of constant  $y$ ).

This sort of flow exhibits long-wavelength instabilities related to the existence of inflection points in the momentum profile at  $y=0$ ,  $y=W/2$ . The critical Reynolds number given by linear stability analysis for infinitely long channels (Kolmogorov flow<sup>30-32</sup>) is quite small,  $R_{cr} \approx 1.11$ , but a finite length-to-width ratio increases  $R_{cr}$ . The particular width-to-length ratio used in our simulation,  $\sqrt{3}/2$ , is linearly stable even for the largest Reynolds number obtainable in our simulation ( $\approx 50$ ), see Appendix B.

The alternative to the double channel with periodic boundary conditions described above would be the use of a single channel with no-slip boundary conditions<sup>12,14</sup> (for instance, random scattering of the particle impinging on the walls) at the upper and lower boundaries. Both simulations dissipate the momentum injected into the gas by the applied body force, but the no-slip condition creates a layer at the boundary (a Knudsen layer<sup>33</sup>) whose thickness is of the order of a mean free path  $l$ . This layer is caused by the matching between the artificial particle distribution externally imposed at the walls and the nonequilibrium particle distributions imposed by the macroscopic flow in the bulk of the fluid. Since  $l$  for our model is typically about three lattice spacings<sup>34</sup> and our channels are only from 32 to 192 lattice rows in width, Knudsen layers along both the upper and lower boundaries would significantly distort the expected parabolic momentum profile, Eq. (6), making it very difficult to detect small corrections to  $\nu$  which depend on the size of the system.

## 2. Momentum profile

Figure 4 shows a typical momentum profile obtained from our simulation. The average number of particles per link in this run is  $d=0.3$ , the system dimensions are  $W=32\sqrt{3}$  and  $L=64$  (corresponding to a  $64 \times 64$  lattice), the forcing level  $F=0.5$  units of momentum per time step, and the collision rules used are described in Fig. 2. The profile was obtained by averaging the microscopic momentum density  $\bar{g}$  in the direction parallel to the flow and on 2 million iterations. The solid line represents a parabola fitted to the simulation results which are shown as symbols. The fit is very good. If we define

$$e(y) = \frac{|\bar{g}_x(y) - h(y)|}{g_x(y)}, \quad (8)$$

where  $h(y)$  is the fitted parabola, then  $\max_y |e(y)| < 6 \times 10^{-3}$ , except for the two outermost rows on each side where  $e(y) < 0.035$  (see Fig. 5). The  $\bar{g}_y$  component appears to be due entirely to statistical noise; it is very small:  $\max_y |\bar{g}_y(y)/\bar{g}_x(y)| < 6 \times 10^{-3}$ , except for the two outermost rows on each side where it is smaller than 0.035.

These results show that our system has a parabolic momentum profile, with a very high accuracy. This result is then a partial justification for the claims of previous authors that this LGA obeys the Navier-Stokes equation. The momentum density profile can be improved by increasing the number of time steps on which the simula-

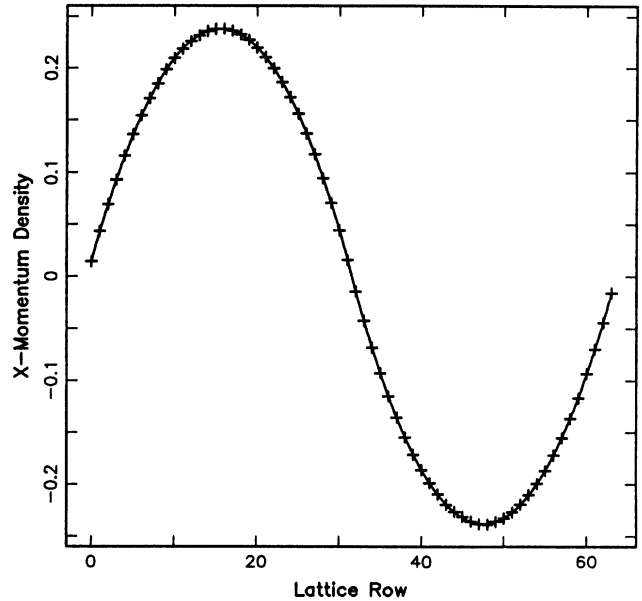


FIG. 4. Typical momentum profile. The  $x$ -momentum density profile for a  $64 \times 64$  system run at reduced density  $d=0.3$  and a forcing level  $F=0.5$  momentum units per time step in each channel. The profile was averaged over 2 million time steps. The solid line is a parabolic fit to the simulation data points (symbols).

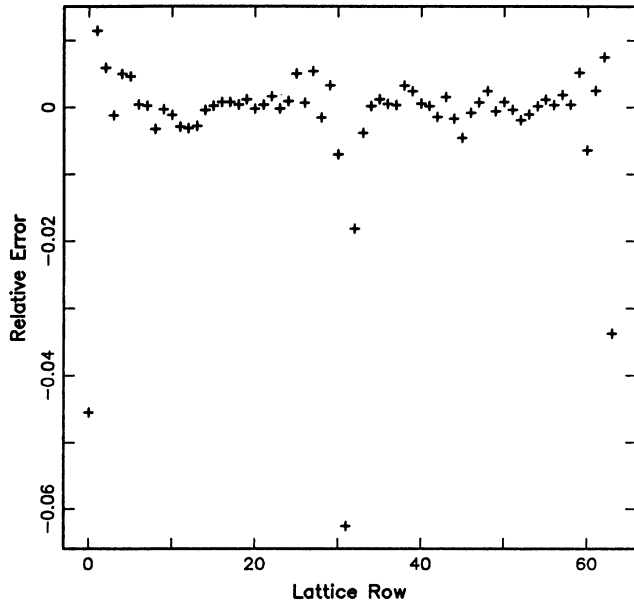


FIG. 5. Relative error for momentum profile. Defined as  $[\bar{g}_x(y) - h(y)]/\bar{g}_x(y)$ , where  $h(y)$  is the solid line and  $\bar{g}_x(y)$  are the simulation data points of Fig. 4.

tion is averaged. However, improvements obtained by averaging are limited by systematic deviations from a parabolic profile, which can only be reduced by decreasing the amplitude of  $\bar{g}$ . These systematic deviations are due to higher-order terms,  $O(\bar{g}^4)$ , neglected in Eq. (5) and to the presence of a term proportional to  $\bar{g}^2$  in Eq. (4). This gives a linear dependence of  $\bar{n}$  in  $\bar{g}^2$  for uniform pressure simulations such as those used in this paper. This effect can be easily observed,<sup>35</sup> and the relation, Eq. (4) checked. In Fig. 6 we compare the slope  $d\bar{n}/d(\bar{g}^2)$  measured in the simulations with that predicted by Eq. (4). A data point is obtained for each reduced density by plotting  $\bar{n}$  versus  $\bar{g}^2$  for various positions across the width of the parabolic momentum profile. The slope of the resulting graph is a quantity, a thermodynamic derivative, which can be computed using only the local equilibrium assumption for the gas. The agreement between theory and experiment is once again excellent, better than 1%. Together with measurements of mean free times between collisions (see also Ref. 22), the results of Figs. 4 and 6 indicate that the gas attained the expected equilibrium.

The results of this section are rather encouraging. The lattice-gas automaton seems to reproduce quite effectively what was predicted by Eq. (6). There is no evidence of discrepancy between the results of the simulations and the prediction of rotational invariance in Eq. (2); also there is no direct evidence of pernicious effects due to the staggered momentum modes.

The lack of Galilean invariance is visible only in the corrections to the number density across the channel and it agrees well with what was predicted by Eq. (4). The distortions to the parabolic profile due to the latter can

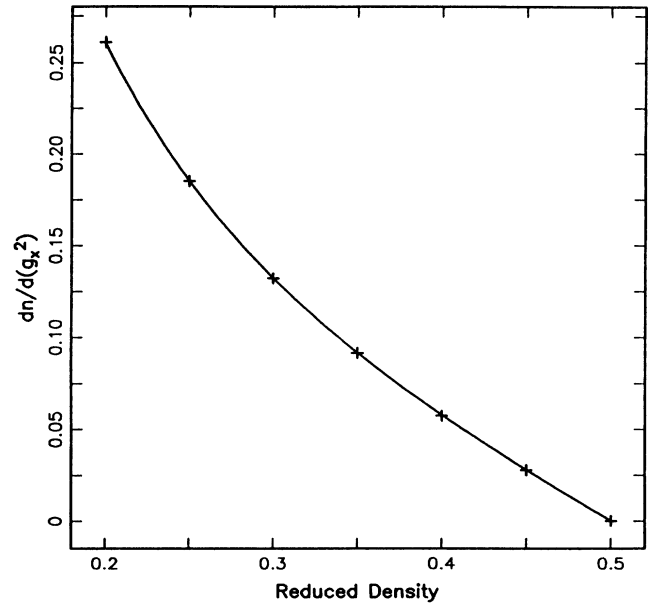


FIG. 6.  $d\bar{n}/d(\bar{g}^2)$ . The simulations are run at constant pressure. This introduces a linear relation between the number density  $\bar{n}$  and the square of the momentum density  $\bar{g}^2$  (see text). We plot the slope measured in the simulations (symbols) for various values of  $d$ . The solid line is obtained from Eq. (4).

be, nevertheless, kept negligible by opportunely choosing low forcing. For the runs discussed in Sec. III we use forcing levels, and therefore  $\bar{g}_x(y)$ , small enough to keep the variation in  $\bar{n}$  across the channel less than 0.2%.

### III. LOGARITHMIC DIVERGENCE

#### A. Mode-mode coupling calculation

In this subsection we will describe our result for the hydrodynamic contribution to the kinematic viscosity of the LGA. The actual calculation follows the line of Ref. 36 and is given in Appendix A.

We start with the assumption that Eqs. (1) and (2) are actually a good description of the dynamic of the hydrodynamic fluctuations of the LGA fluid. In particular, we deduce from Eq. (2) that a small amplitude fluctuation of wave vector  $\mathbf{q}$  will quickly relax<sup>37</sup> into six modes. The first two are sound waves with a complex “decay rate:”

$$s_{\pm} = \pm icq + \Gamma q^2, \quad (9)$$

where the sound damping coefficient  $\Gamma$  is given by  $\Gamma = \frac{1}{2}(\nu + \zeta)$ . The third is a transverse mode with decay rate

$$s_1 = \nu q^2, \quad (10)$$

and finally there are three hydrodynamic modes describing the diffusion of the staggered momentum densities. Their decay rates are given by

$$s_{\alpha} = \kappa_{\alpha}(\hat{\mathbf{q}})q^2 = [\kappa_1 + \kappa_2(\mathbf{C}_{\alpha} \cdot \hat{\mathbf{q}})^2]q^2, \quad (11)$$

where  $\hat{\mathbf{q}}$  is the unit vector along the direction of  $\mathbf{q}$ . The kinematic viscosity for the LGA fluid can be given in terms of a Green-Kubo expression, equivalent to the one found by Frisch and Rivet in Ref. 38,

$$\nu = \frac{1}{\chi_1} \sum_{\mathbf{r} \in \Omega} \sum_{t=0}^{\infty} \langle\langle \Pi_{xy}(0,0) \Pi_{xy}(t,\mathbf{r}) \rangle\rangle + \nu_p. \quad (12)$$

The sum in  $\mathbf{r}$  is on the finite region of the lattice considered ( $\Omega$  will indicate both the region and its volume); the  $\langle\langle \rangle\rangle$  indicates the equilibrium average on the grand-canonical ensemble consistent with average density per site of  $7d$  and  $\langle\langle g \rangle\rangle = \langle\langle h \rangle\rangle = 0$ . Here,  $\chi_1$  is the momentum density susceptibility, explicitly  $\chi_1 = 3d(1-d)$ , defined by the derivative of the macroscopic momentum density with respect to the intensive parameter conjugate to the momentum density  $\partial\langle\langle g_i \rangle\rangle/\partial\gamma_j$ , or equivalently as the equal time momentum autocorrelation function. The quantity  $\Pi_{xy}$  is the off-diagonal term of the microscopic stress tensor, defined as the sum

$$\Pi_{ij} = \sum_{\alpha} C_{\alpha,i} C_{\alpha,j} f_{\alpha}(\mathbf{r}).$$

$$\nu(L) = \nu_0 + \frac{1}{2\chi_1^3} \left[ \frac{\partial\langle\langle \Pi_{xy} \rangle\rangle}{\partial\gamma_x \partial\gamma_y} \right]^2 \left[ \left[ \frac{2}{\nu(L)} + \frac{1}{\Gamma(L)} \right] \frac{1}{N} \sum_{L^{-1} \leq q \leq a^{-1}} \frac{q_x^2 q_y^2}{q^6} + \frac{3}{4} \frac{1}{N} \sum_{L^{-1} \leq q \leq a^{-1}} \frac{1}{\kappa(\hat{\mathbf{q}}) q^2} \right], \quad (13)$$

where  $\nu_0$  is the part of the kinematic viscosity that we have not explicitly considered but which is assumed not to depend on  $L$ . In the above expression the sum on the reciprocal lattice has  $a^{-1}$  as the ultraviolet cutoff and we have inserted as infrared cutoff the typical linear size of the system  $L \approx \sqrt{\Omega}$ . If the linear dimensions of the system are enlarged by a factor  $e^b$  with  $b$  small, the previous formula would predict, for large  $L$ , a change in viscosity:

$$\begin{aligned} \nu(e^b L) - \nu(L) = & \frac{(1-2d)^2}{96d(1-d)} \left[ \frac{2}{\nu(L)} + \frac{1}{\Gamma(L)} \right. \\ & \left. + \frac{6}{\kappa_1} \frac{1}{\sqrt{1+\kappa_2/\kappa_1}} \right] \\ & \times \frac{\Omega}{N} \frac{1}{16\pi} b, \end{aligned} \quad (14)$$

where  $\Omega = (\sqrt{3}/2)N$  is the volume of the system, and we have substituted for all the thermodynamic derivatives their explicit expressions (see Appendix A). In principle, we should integrate Eq. (13) and its equivalent for  $\Gamma$ ,  $\kappa_1$ , and  $\kappa_2$  to obtain the transport coefficients as functions of  $\ln(L)$ .

Using our channel flow we are able to measure the kinematic viscosity  $\nu$  with good accuracy. Unfortunately we were not able to devise an equivalent steady-flow scheme for the measurement of the other transport coefficients. We obtained reasonably accurate values for the latter by using relaxation measurements similar to the

Finally,  $\nu_p$  ( $= -\frac{1}{8}$ ) is a contribution to the viscosity only due to the discreteness of the lattice<sup>39</sup> that, since it is not relevant for the following calculations, we will henceforth neglect.

Equation (12) relates the kinematic viscosity to a sum on the two-point correlation function of the stress tensor. To find this correlation function is a rather difficult many-body problem. Following Ref. 36 we assume that the hydrodynamic contribution to the transport coefficient can be written in terms of projections of the microscopic stress tensor on intermediate long-wavelength multitransport modes that are constructed as products of hydrodynamic modes and whose decay rate is given by the sum of the decay rates, Eqs. (9) and (11), of the component modes. We will consider only two-coupled mode contributions, since it is possible to show that the terms involving three or more modes do not contribute to the asymptotically dominant logarithmic divergence. The vertices relevant to the calculation are the projection of the stress tensor on the sound-sound, transverse-transverse, and coupled staggered momentum diffusion modes. They can be readily evaluated (see Appendix A), and after inserting the result in Eq. (12), we obtain

ones described in Ref. 40. However, the values thus obtained cannot be used in Eq. (14) since the relaxation time scale is not long enough for the buildup of the hydrodynamic corrections. To compensate for this we multiply the value of the transport coefficients obtained from the relaxation measurement by  $\nu(L_1)/\nu_r$ , where  $\nu_r$  is the kinematic viscosity obtained by the relaxation measurement. This is a completely heuristic procedure. It, however, seems a reasonable assumption.

In conclusion, we predict a linear<sup>41</sup> growth for  $\nu$  in the range of  $L$  considered, with slope

$$\begin{aligned} \frac{d\nu}{d \ln L} = & \frac{\sqrt{3}(1-2d)^2}{3072\pi d(1-d)} \\ & \times \left[ \frac{2}{\nu_{L_1}} + \frac{\nu_r}{\nu_{L_1}} \left[ \frac{1}{\Gamma_r} + \frac{6}{\kappa_{1r}} \frac{1}{\sqrt{1+\kappa_{2r}/\kappa_{1r}}} \right] \right]. \end{aligned} \quad (15)$$

Note that the divergent term in the viscosity given by Eq. (15) is zero for  $d = \frac{1}{2}$ . This is not surprising since the nonlinearity of the convective term of the stress tensor, Eq. (2), is the source of the coupling to the multitransport modes, and we already noted that the coefficient  $\lambda(d)$  multiplying the convective and other nonlinear terms is also zero for  $d = \frac{1}{2}$ .<sup>28</sup>

## B. Simulation results

In this section we describe the results of the viscosity measurement for various channel sizes. The results we present are the distillate of about 150 runs. Each simulation ran for 1–4 million time steps. For each run we estimate an error in the measured  $\nu$  as described in Appendix C. The measured kinematic viscosity does indeed depend on  $L$  and the increment in  $\nu$  due to the channel enlargement is consistent with the prediction of Eq. (15).

### 1. Viscosity as a function of the forcing level

We do not measure any apparent dependence of the kinematic viscosity, for a fixed channel width and reduced density, on the forcing level. Within the “experimental errors,” runs with different forcing levels give the same  $\nu$ .

It goes without saying that the range of forcing levels possible in the simulations is very small; for too weak forcing the time averaging required to damp the statistical noise becomes prohibitive and for too strong forcing the distortion to the parabolic profile due, for instance, to mass redistribution makes the measure meaningless. However, we ran each channel simulation for four forcing levels with the largest forcing used 2.5 times the smallest.

### 2. Viscosity as a function of $L$

In Fig. 7 we depict  $\nu$  as a function of  $L$ . The reduced density used is 0.2, and the viscosity points are obtained as weighted averages of numerous runs for each  $L$  value, with different initial conditions and forcing levels. The

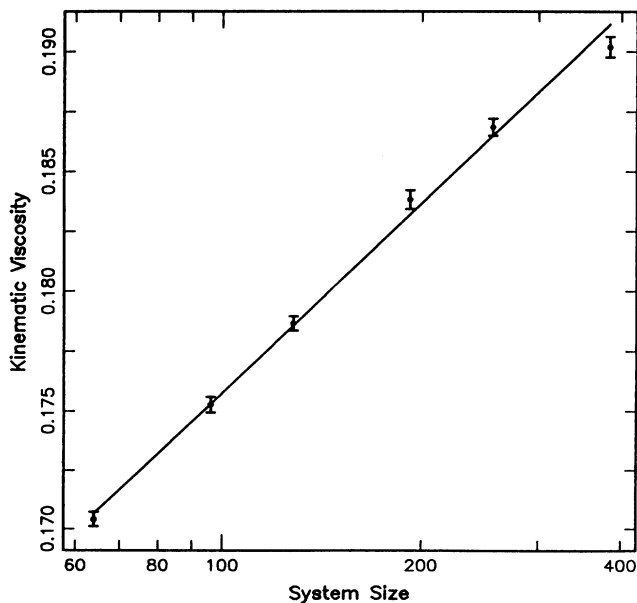


FIG. 7. The kinematic viscosity as a function of the system size. The reduced density for the data shown is  $d=0.2$ . The error bars are obtained by comparisons between different runs and the solid line is obtained from a weighted fit.

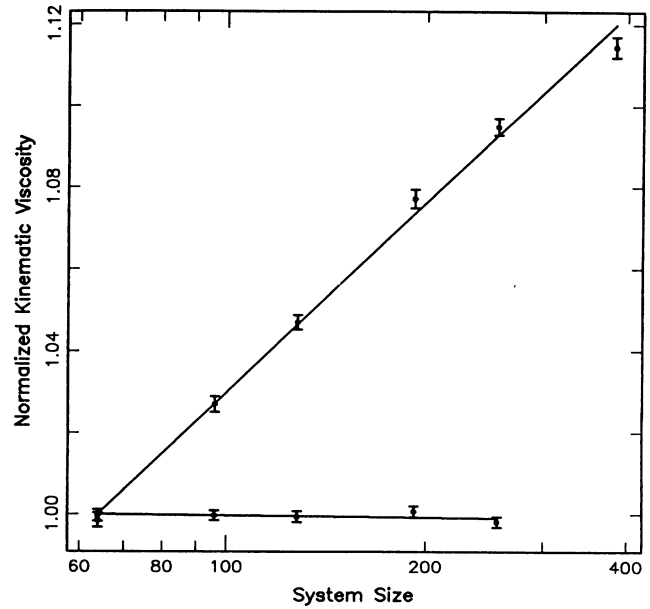


FIG. 8. Normalized kinematic viscosity as a function of the system size  $L$ . We show two sets of kinematic viscosity data,  $d=0.2$  and 0.5, normalized by the value of  $\nu$  at  $L=64$ . The solid lines are weighted fits to the two sets of data.

effective viscosity increases with  $L$  and, in a linear-logarithmic plot, the curve appears to be linear. As a qualitative test for the consistency of this effect with Eq. (15) we again plot the viscosity, Fig. 8 (this time normalized with its value at  $L=32$ ), as a function of  $L$  for  $d=0.2$  and 0.5. As expected,  $d=0.5$  gives no  $L$ -dependent term in the viscosity. Thus we conclude that boundary corrections, such as those of Knudsen, proportional to  $(l/L)$ , do not explain our observed dependence of  $\nu$  upon  $L$ , and neither do possible staggered momentum density effects since, as we argue in Appendix D, they will give contributions proportional to  $1/L^2$ .

### 3. Viscosity as a function of the density

We have performed the same viscosity measurement for various values of the reduced density. The range of  $d$  explored is 0.2–0.5 in steps of 0.05. Figure 9 shows the measured viscosities as a function of  $d$  for various values of the channel size. The solid line is the value of the kinematic viscosity predicted by the Chapman-Enskog calculation<sup>22,42</sup> for the collision rules of Fig. 2.

### 4. Comparison between the mode-mode coupling result and simulation data

The last and most interesting figure we present is a comparison between the slopes of linear fits to the  $\nu$  versus  $\ln(L)$  data for various values of  $d$  and the mode-mode coupling prediction, Eq. (15). The symbols in Fig. 10 are the experimental values, while the solid line is given by Eq. (15). The error bars reported are obtained by propagating the errors on the single viscosity measure-

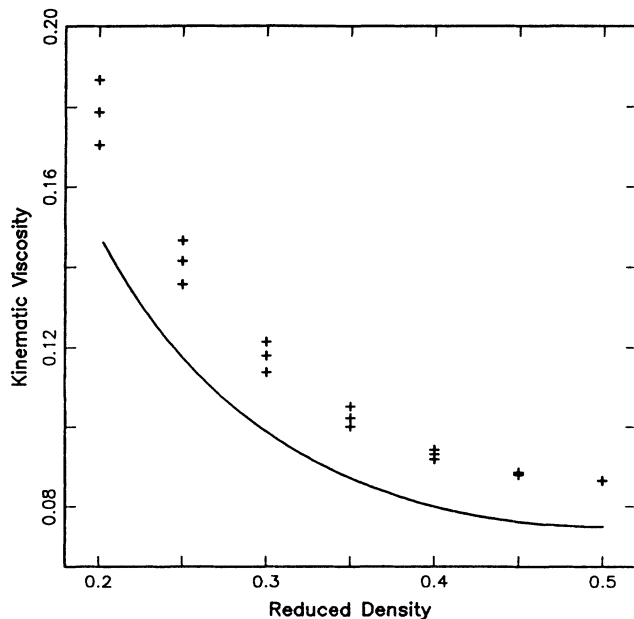


FIG. 9. Kinematic viscosity as a function of the reduced density. The three sets of symbols are obtained from measurements on systems of size  $L = 64, 128,$  and  $256$ . For a given reduced density the viscosity is increasing with channel size. The estimated errors are smaller than the symbols used in the plot.

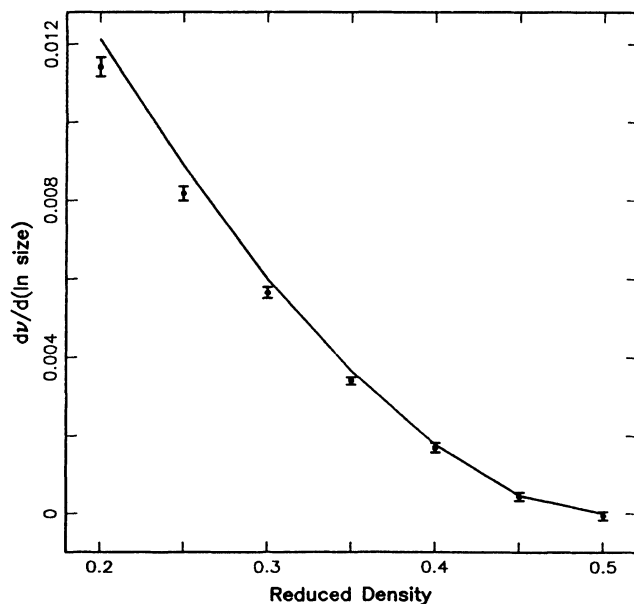


FIG. 10.  $dv/d\ln L$  as a function of the reduced density  $d$ . The solid curve is from Eq. (15) while the simulation data (symbols) are the slopes obtained from weighted fits like that shown in Fig. 6.

ments done at each density value and channel width. For a given density we fitted a straight line on all the viscosity points we had. Hence the reported measured slopes are presumably affected by finite-size corrections to the asymptotic law, Eq. (15), and the error bars in Fig. 10 are only indicative of our numerical errors and not of our (unknown) systematic errors. The fit is reasonably good. It is, however, clear that there is a systematic effect; all the measured points are below the theoretical curve. We have not been able to explain this discrepancy. It could have a rather prosaic origin, e.g., the  $v(L)/v_r$  correction used in Eq. (15) could be an underestimate of the hydrodynamic corrections on the other  $\Gamma, \kappa_1, \kappa_2$  transport coefficient, or higher-order perturbative effect neglected in our theory. It could, however, be something deeper, e.g., some mischievous side effect due to the staggered momentum modes.

#### IV. CONCLUSIONS

We think that Figs. 4, 6, and 10 are good indications that Eqs. (1)–(4) give, at least under the simulation conditions described in this paper, an accurate description of the dynamical property of the lattice-gas automata. The most important result is contained in Fig. 10. The solid curve is a compendium of various of the gas's assumed dynamical and thermodynamical equilibrium properties with assumptions on the nature of the essential mechanism for the divergence of  $v$  (intermediate long-wavelength multitransport modes). The agreement between this curve and the simulation results can be read in two directions. The first takes for granted the prediction of the mode-mode coupling calculation, Eq. (15), and effectively tests if the long-wavelength dynamics of the gas is controlled by the conservation laws, Eqs. (1)–(4). The second, in the same spirit as the molecular-dynamics simulations,<sup>21,19</sup> takes the LGA as a two-dimensional fluid of well-known properties and uses it as a tool to give a simulative verification of Eq. (15). The LGA, from the last point of view, is a very efficient tool.

Why is this so? The lattice-gas automaton is very noisy (Appendix C). This is a source of problems when it is applied to the solution of the incompressible Navier-Stokes equation<sup>26,35</sup> but it is an advantage in our case since it enhances the thermodynamic derivative in the coefficient of Eq. (13). Moreover, the collision rules used in our simulation give small transport coefficients [i.e., a small denominator in Eq. (13)] and very short particle mean free paths. With very short mean free paths it is possible to have a good local equilibrium description even with small simulation systems (e.g.,  $L = 64$ ) and thus it is possible to investigate a reasonable range of system sizes without going toward systems that are too large to simulate.

All in all, we do believe that we have shown that the LGA does simulate hydrodynamic equations, and that the actual equations obeyed are potentially more complex than the Navier-Stokes equation.

#### ACKNOWLEDGMENTS

We have the pleasure to thank D. d'Humieres, G. Doolen, U. Frisch, B. Hasslacher, Y. Pomeau, and S.

Zaleski for interesting and fruitful discussions, and G. Doolen and T. Shimomura for the original version of the FORTRAN program we have used. We would like to express our gratitude for the help of IBM. In addition, we would like to thank Albert Crewe for providing both advice and material help. This work was supported by the U.S. Office of Naval Research, the Division of Materials Research, National Science Foundation, and by a grant of computer time from the National Center for Supercomputing Applications. We gratefully acknowledge the hospitality of the Los Alamos National Laboratory where a portion of this work was done.

### APPENDIX A

In this appendix we will derive Eq. (13) of Sec. III. The calculation is a straightforward application of the method illustrated in Ref. 36. The only modification is the translation of the relevant thermodynamic derivatives into the language of lattice-gas automata. This is rather easy because the equilibrium probability distribution for the lattice-gas automaton factorizes on the sites and directions in the product of one-particle equilibrium distributions. The latter property is essential for the local equilibrium description of the gas and hence for the derivation of Eq. (2) and it guarantees that the particle populations at different sites and/or directions are completely uncorrelated, i.e.,

$$\langle\langle [f_a(\mathbf{r}) - d_a][f_{a'}(\mathbf{r}') - d_{a'}] \rangle\rangle = d_a(1 - d_a)\delta_{aa'}\delta_{\mathbf{r}\mathbf{r}'}, \quad (\text{A1})$$

where  $d_a = \langle\langle f_a \rangle\rangle$ .

As a first step in obtaining Eq. (12) we explicitly write the Fourier transform of the microscopic fluctuations around  $\langle\langle n \rangle\rangle = 7d$ ,  $\langle\langle g_l \rangle\rangle = \langle\langle h_a \rangle\rangle = 0$ :

$$n(\mathbf{q}) = \frac{1}{\sqrt{N}} \sum_{\mathbf{r} \in \Omega} e^{-i\mathbf{q}\cdot\mathbf{r}} n(\mathbf{r}), \quad (\text{A2})$$

$$g_m(\mathbf{q}) = \frac{1}{\sqrt{N}} \sum_{\mathbf{r} \in \Omega} e^{-i\mathbf{q}\cdot\mathbf{r}} g_m(\mathbf{r}), \quad (\text{A3})$$

$$h_a(\mathbf{q}) = \frac{1}{\sqrt{N}} \sum_{\mathbf{r} \in \Omega} e^{-i\mathbf{q}\cdot\mathbf{r}} h_a(\mathbf{r}). \quad (\text{A4})$$

In the long-wavelength limit we expect them to be controlled by the hydrodynamic equations, Eqs. (1)–(4), and hence to have a natural description, for a given wave vec-

$$\hat{\Psi}_{a,\dots,a'}(q,\dots,q') = \frac{\hat{\Psi}_a(q) \cdots \hat{\Psi}_{a'}(q') - \langle\langle \hat{\Psi}_a(q) \cdots \hat{\Psi}_{a'}(q') \rangle\rangle}{[\langle\langle \hat{\Psi}_a(q) \cdots \hat{\Psi}_{a'}(q') | \hat{\Psi}_a(q) \cdots \hat{\Psi}_{a'}(q') \rangle\rangle - \langle\langle \hat{\Psi}_a(q) \cdots \hat{\Psi}_{a'}(q') \rangle\rangle^2]^{1/2}}, \quad (\text{A10})$$

where the indices  $a, \dots, a'$  run over  $\perp, +, -, \alpha$ . The transport processes coupled together in Eq. (A10) are, up to cross terms  $\mathcal{O}(1/N)$ , independent (at equilibrium all the sites are decorrelated). Hence their decay rates can be estimated as the sum of the decay rates of the component transport modes:

$$s_{a,\dots,a'}(q,\dots,q') = s_a(q) + \cdots + s_{a'}(q'). \quad (\text{A11})$$

tor  $\mathbf{q}$ , in terms of a transverse mode  $\hat{\Psi}_\perp(\mathbf{q})$ , two sound waves  $\hat{\Psi}_\pm$ , and three staggered momentum modes,  $\hat{\Psi}_\alpha$ ,  $\alpha=0, 1, 2$  defined by

$$\begin{aligned} \hat{\Psi}_\pm(q) &= \frac{1}{\sqrt{2\chi_1}} [c\hat{n}(q) \pm \hat{g}_\parallel(q)], \\ \hat{g}_\parallel(q) &= q^{-1} [q_x \hat{g}_x(q) + q_y \hat{g}_y(q)], \end{aligned} \quad (\text{A5})$$

with decay rates

$$s_\pm = \pm icq + \Gamma q^2, \quad (\text{A6})$$

where the sound damping coefficient  $\Gamma$  is given by  $\Gamma = \frac{1}{2}(\nu + \zeta)$ ; the transverse mode

$$\begin{aligned} \hat{\Psi}_\perp(q) &= \frac{1}{\sqrt{\chi_1}} \hat{g}_\perp(q), \\ \hat{g}_\perp(q) &= q^{-1} [-q_y \hat{g}_x(q) + q_x \hat{g}_y(q)], \end{aligned} \quad (\text{A7})$$

with decay rate

$$s_\perp = \nu q^2; \quad (\text{A8})$$

and the staggered momentum modes

$$\hat{\Psi}_\alpha(q) = \frac{1}{\sqrt{\chi_1}} \hat{h}_\alpha(q), \quad (\text{A9})$$

with decay rates

$$s_\alpha = \kappa_\alpha(\hat{\mathbf{q}})q^2 = [\kappa_1 + \kappa_2(\mathbf{C}\cdot\hat{\mathbf{q}})]q^2.$$

The  $\hat{\Psi}_a$  ( $a = \perp, +, -, \alpha$ ) defined above are normalized to 1,  $\langle\langle \hat{\Psi}_a | \hat{\Psi}_a \rangle\rangle = 1$ , where we have introduced the scalar product<sup>36</sup>  $\langle\langle f | g \rangle\rangle = \langle\langle \hat{f}g \rangle\rangle$ . The coefficient  $\chi_1$  inserted in Eqs. (A5) and (A7) is defined by  $\langle\langle \hat{g}_l(q) | \hat{g}_m(q') \rangle\rangle = \chi_1 \delta_{lm} \delta_{qq'}$  while  $c = \sqrt{\chi_1/\chi_0}$  is the speed of sound for the gas with  $\langle\langle \hat{n}(q) | \hat{n}(q') \rangle\rangle = \chi_0 \delta_{qq'}$ . It is easy to see, using Eq. (A1), that  $\chi_0 = 7d(1-d)$  and  $\chi_1 = 3d(1-d)$ .

The modes  $\hat{\Psi}_a$  cannot be directly used to explain the long-time behavior of the integrand in Eq. (11). In fact, in Eq. (11) the correlation function in the integrand is really the correlation function of the part of the microscopic currents orthogonal to the transport modes  $\hat{\Psi}_a$ . In Eq. (11) it is not necessary to write the projection explicitly because  $\Pi_{xy}$  is already orthogonal to the  $\hat{\Psi}_a$ .<sup>36</sup> On the other hand, the  $\hat{\Psi}_a$  are not the only slow processes possible. In particular, we can consider multitransport modes,  $\hat{\Psi}_{a,\dots,a'}(q,\dots,q')$ , as intermediate processes. They are built as products of the transport modes

We rewrite Eq. (11), using translational invariance, as

$$\nu = \frac{1}{\chi_1} \frac{1}{N} \sum_{t=0}^{\infty} \langle\langle \hat{\Pi}_{xy}(0,0) \hat{\Pi}_{xy}(t,0) \rangle\rangle + \nu_p, \quad (\text{A12})$$

where  $\hat{\Pi}_{xy}(t,\mathbf{q})$  is the discrete Fourier transform of the microscopic stress tensor. The structure, Eq. (A11), of the coupled modes suggests writing Eq. (A12) as

$$v = v_0 + \left\langle \hat{\Pi}_{xy}(0,0) \left| \left[ \frac{1}{2!} \sum_{a,a'} \frac{|a,a';q,-q\rangle \langle a,a';q,-q|}{s_a(q) + s_{a'}(-q)} + \frac{1}{3!} \sum_{a,a',a''} \frac{|a,a',a'';q,q',-q-q'\rangle \langle a,a',a'';q,q',-q-q'|}{s_a(q) + s_{a'}(q) + s_{a''}(-q-q')} + \dots \right] \hat{\Pi}_{xy}(0,0) \right\rangle, \quad (\text{A13})$$

where the indices  $a, \dots, a'$  run over  $+, -, \perp$ , and  $\alpha$  as above, and where we have already performed the time summation.<sup>43</sup>

We will consider only the first order in the perturbation calculation, i.e., only the contribution of two-coupled transport modes, because the higher-order diagrams give finite contributions. The vertices relevant to the calculation, sound-sound, transverse-transverse modes, and coupled staggered momentum<sup>44</sup> can be easily calculated starting from

$$\begin{aligned} \langle \hat{\Pi}_{xy}(0) | \hat{g}_l(q) \hat{g}_m(-q) \rangle &= \frac{1}{N^{3/2}} \sum_{\alpha, \alpha', \alpha''} C_{\alpha;x} C_{\alpha;y} C_{\alpha';l} C_{\alpha'';m} \sum_{r,r',r''} e^{-iq \cdot (r' - r'')} \langle [f_\alpha(\mathbf{r}) - d][f_{\alpha'}(\mathbf{r}') - d][f_{\alpha''}(\mathbf{r}'') - d] \rangle \\ &= \frac{3d(1-d)(1-2d)}{4\sqrt{N}} (\delta_{xl} \delta_{ym} + \delta_{xm} \delta_{yl}), \end{aligned} \quad (\text{A14})$$

where we used Eq. (A1) and the definition Eq. (A3). From Eq. (A14) and the previous definitions we obtain

$$\langle \hat{\Pi}_{xy}(0) | \perp, \perp; q, -q \rangle = \frac{(1-2d)}{2\sqrt{N}} \frac{q_x q_y}{q^2}, \quad (\text{A15})$$

$$\begin{aligned} \langle \hat{\Pi}_{xy}(0) | +, +; q, -q \rangle &= \langle \hat{\Pi}_{xy}(0) | -, -; q, -q \rangle \\ &= -\frac{(1-2d)}{4\sqrt{N}} \frac{q_x q_y}{q^2}, \end{aligned} \quad (\text{A16})$$

$$\langle \hat{\Pi}_{xy}(0) | \alpha, \alpha; q, -q \rangle = \frac{(1-2d)}{2\sqrt{N}} C_{\alpha;x}^1 C_{\alpha;y}^1. \quad (\text{A17})$$

Inserting Eqs. (A15)–(A17) in Eq. (A13) gives then Eq. (13) of Sec. III.

## APPENDIX B

In this appendix we discuss the linear stability of the parabolic profile, Eq. (6). It is sufficient to study the linear stability of the unidirectional steady solution of Eq. (5) with the periodic “square-wave” force field of amplitude  $A$  and wavelength  $2W$  given by

$$\mathbf{f}^*(x,y) = \begin{cases} (A, 0) & \text{for } 2nW \leq y < (2n+1)W, \\ (-A, 0) & \text{for } (2n+1)W \leq y < 2(n+1)W, \end{cases} \quad (\text{B1})$$

with  $n$  integral. For time-dependent incompressible flow, Eq. (5) becomes

$$\begin{aligned} \partial_k g_k &= 0, \\ \partial_l g_l + g_k \partial_k g_l &= -\partial_l p + R^{-1}(\partial_k \partial_k g_l + f_l). \end{aligned} \quad (\text{B2})$$

In Eq. (B2) and in the rest of this appendix we will use  $\mathbf{g}$ ,  $t$ ,  $\mathbf{r}$ ,  $p$ , and  $\mathbf{f}$  to indicate the nondimensional momentum density, time, position vector, pressure, and force density, respectively. To write Eq. (B2) in nondimensional form we use  $(2W)$  as the unit of length,  $G = [A(2W)^2]/\nu$  as the unit of momentum density, and  $T = (2W)/(\lambda G)$  as the unit of time.  $R$  is then the “Reynolds” number

$$R = \frac{\lambda 2WG}{\nu}. \quad (\text{B3})$$

The  $R$  thus defined is 32 times larger than the “natural” Reynolds number,  $\bar{R} = \lambda(2W)\bar{g}_{\max}/\nu$  [cf. Eq. (7)]. Hence the maximal  $R$  considered in our simulation becomes  $R \approx 1500$ .

The viscous flow solution of Eq. (B2),

$$\begin{aligned} g_y(x,y) &= 0, \\ g_x(x,y) &= \begin{cases} +\frac{1}{2}(y-n)(n+\frac{1}{2}-y) & \text{for } n \leq y < n+\frac{1}{2}, \\ -\frac{1}{2}(y-n-1)(n+1-y) & \text{for } n+\frac{1}{2} \leq y < n+1, \end{cases} \end{aligned} \quad (\text{B4})$$

is for large  $R$  linearly unstable with respect to long-wavelength perturbations parallel to the “channel” axis. An asymptotic calculation<sup>45</sup> gives as the critical value of the Reynolds number

$$R_{\text{cr}} = 3 \times 64 \sqrt{35/17}. \quad (\text{B5})$$

The critical Reynolds number, Eq. (B5), is valid for an infinitely long channel where modes of arbitrary long wavelength can be excited. However, for a channel (such as the one depicted in Fig. 1) with a finite length-to-width ratio,  $\beta = (2W)/L$ , there is an infrared cutoff on the possible perturbations and thus an increase in the critical Reynolds number. We want to show that the channel used in the simulation, for which  $\beta = \sqrt{3}/2$ , is linearly stable in the range of  $R$  used. Since the flow is incompressible we will write the nondimensional momentum density field  $g_l$  in terms of a stream function  $\psi$ ,

$$\begin{aligned} g_x &= -\partial_y \psi, \\ g_y &= \partial_x \psi. \end{aligned} \quad (\text{B6})$$

We now write  $\psi$  as the sum of a small perturbation  $\phi$  to  $\psi_0$ , which is the stream function corresponding to the

unidirectional steady solution, Eq. (B4). Equation (B2) can now be linearized around  $\psi_0$ , and, after some standard manipulation, the result is

$$\Delta \partial_t \phi = [a \Delta - (\Delta a)] \partial_x \phi + R^{-1} \Delta^2 \phi, \quad (\text{B7})$$

where  $\Delta$  is the Laplacian operator,  $\Delta = (\partial_x^2 + \partial_y^2)$ , and  $a = \partial_y \psi_0$ . We will now use the periodicity of the channel to write

$$\psi_0(x, y) = \sum_{m=-\infty}^{m=\infty} \psi_{0,m} e^{i2\pi m y}, \quad (\text{B8})$$

$$\phi(x, y) = \sum_{n,m=-\infty}^{n,m=\infty} \phi_{n,m} e^{i2\pi(n\beta x + m y)}.$$

Thus we can rewrite Eq. (B7) as

$$\begin{aligned} \frac{1}{(2\pi)^2} \frac{d\phi_{n,m}}{dt} = \sum_{m'} (U_{mm'}^n) \phi_{nm'} = -R^{-1} (\beta^2 n^2 + m^2) \phi_{n,m} \\ + \frac{\beta n}{\beta^2 n^2 + m^2} \sum_{m'} \psi_{0,m-m'} (m-m') \{ [\beta^2 n^2 + (m')^2] - (m-m')^2 \} \phi_{n,m'} \end{aligned} \quad (\text{B9})$$

We then notice that  $n$  labels the eigenspaces of Eq. (B7). Moreover,  $n$  always appears in Eq. (B9) in the combination  $(\beta n)$ . Thus

$$(U_{mm'}^{n'}(\beta, R)) = (U_{mm'}^n(n'\beta/n, R)). \quad (\text{B10})$$

Hence we have reduced the problem to a discussion of the eigenvalues of the matrix  $(U_{mm'}^1)$ . Using the explicit expression for  $\psi_{0,m}$ ,

$$\psi_{0,m} = \begin{cases} 0 & \text{for } m=0, \\ -\frac{4 \sin^2(\pi m/2)}{(2\pi m)^4} & \text{otherwise,} \end{cases} \quad (\text{B11})$$

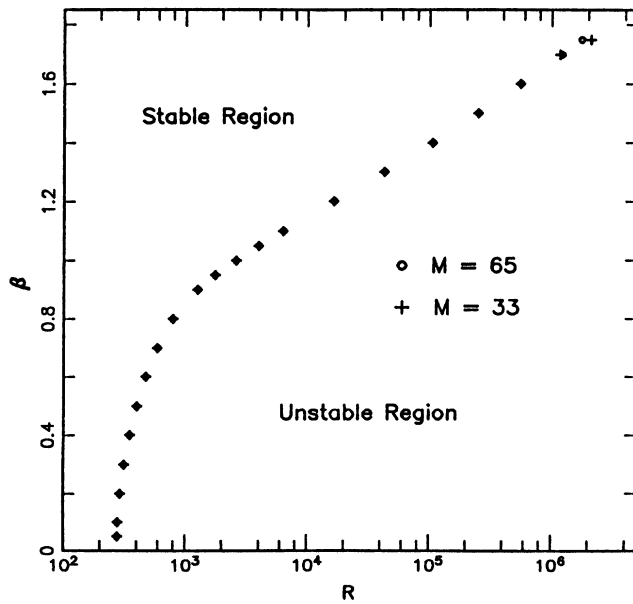


FIG. 11. Stability curve for the forced flow. The two sets of symbols correspond to different values of  $M$  ( $M=33, 65$ ), the number of modes at which  $(U_{mm'}^1)$  has been truncated. In the region marked stable (unstable)  $\mu^*$  is negative (positive).

we can write

$$\begin{aligned} U_{mm'}^1 = -R^{-1} \delta_{mm'} (\beta^2 + m^2) \\ + \frac{4\beta \sin^2[\pi(m-m')/2]}{(2\pi)^4 (\beta^2 + m^2)(m-m')^3} \\ \times \{ (m-m')^2 - [\beta^2 + (m')^2] \}. \end{aligned} \quad (\text{B12})$$

We consider now only a finite number of “modes” in Eq. (B9), i.e.,  $-M \leq m \leq M$  and then study numerically the eigenvalues of the truncated matrix  $(\tilde{U}_{mm'}^1)$ . We are interested in the sign of

$$\mu^*(\beta, R, M) = \max\{\text{Re}\mu; \mu \text{ eigenvalue of } (\tilde{U}_{mm'}^1)\},$$

( $\text{Re}\mu$  is the real part of  $\mu$ ). In Fig. 11 we show the stability curve,  $R^* = R^*(\beta)$ , in the  $\beta, R$  parameter plane. The points marked in the figure correspond to  $R^*(\beta)$  and are obtained by solving numerically  $\mu^*[\beta, R^*(\beta), M] = 0$  while keeping  $M$  fixed. To test how the result depends on  $M$ , we show two sets of symbols corresponding to  $M=33, 65$ . For  $R < 10^5$  the two sets of points agree within one part in  $10^4$ .

In the limit of  $\beta \rightarrow 0$ ,  $R^*(\beta)$  converges to the  $R_{cr}$  given in Eq. (B5). Moreover, the values of  $R$  considered in our simulation ( $\beta = \sqrt{3}/2$ ) are all well within the stable region of  $(U_{mm'}^1)$ . Using Eq. (B10) we can extend this stability result to other values of  $n, n > 1$ . We conclude that in the range of  $R$  used in our simulation the channel flow is stable.

### APPENDIX C

The measured  $v$  is obtained by Eq. (7) and the quantity actually measured in the simulations is a time average of  $\bar{g}_{\max}$ . The latter is proportional to

$$\bar{g}_{\text{av}} = \frac{1}{TL^2} \sum_{t=1}^{t=T} \sum_{x,y=1}^{x,y=L} g_x(x, y; t). \quad (\text{C1})$$

The goal of this appendix is to give some estimates of the standard deviation of  $\bar{g}_{\text{av}}$ .

$$\langle\langle (\delta\bar{g}_{av})^2 \rangle\rangle = \left[ \frac{1}{TL^2} \right]^2 \sum_{t,t'=1}^{t,t'=T} \sum [g(x,y;t) - \bar{g}(x,y)][g(x',y';t') - \bar{g}(x',y')] . \quad (C2)$$

The lattice gas is extremely noisy; at thermodynamic equilibrium and for small values of the average microscopic momentum density, the mean-square average of the microscopic momentum density fluctuation is well approximated by its value for  $\langle\langle g \rangle\rangle = 0$  [see Eq. (A1)]:

$$\langle\langle (\delta g)^2 \rangle\rangle = 3d(1-d) . \quad (C3)$$

Thus to obtain sensible results  $g$  should be averaged over large regions of the lattice and over long times. In the following considerations we assume that the grand canonical ensemble result, Eq. (C3), holds, and for simplicity we take all the average values to be zero.

Consider, in Eq. (C2), the sum on the lattice first. For any given time step, we consider all lattice sites to be uncorrelated<sup>46</sup> thus we can approximate

$$\left[ \frac{1}{L^2} \sum_{x,y=1}^{x,y=L} g_x(x,y) \right]^2 \approx \frac{3d(1-d)}{L^2} . \quad (C4)$$

For the remaining time sum, we can assume that the quantity  $\sum_{x,y} g_x(x,y;t)$  becomes uncorrelated after an interval of the order of the diffusion time on a distance  $L$ ; therefore

$$\langle\langle (\delta\bar{g}_{av})^2 \rangle\rangle \approx \frac{3d(1-d)}{Tv} . \quad (C5)$$

Thus the statistical error on  $v$  does not depend on the channel size but rather on the number of time steps on which the parabolic profile has been averaged. We have compared formula (C5) with the results of extensive simulation of an unforced channel for various values of the density and system size and found good agreement (about 1%). Hence we used Eq. (C5) to estimate the statistical errors on the various viscosity measurements we report.

#### APPENDIX D

The forcing scheme described in Sec. II B 1 is an attempt to impose on the system a square-wave force field. It is designed so that it will act with the same probability on all the lattice sites, but it is necessarily discrete. As a consequence we not only transfer momentum to the fluid but we also excite the  $h_2$  and  $h_3$  modes (the forcing is applied along the  $x$  direction and thus the resulting projection on the  $h_1$  mode is identically null). The nonzero value of the average staggered momentum density will then modify the constitutive relations of Eq. (2) since they were obtained as an expansion around  $h_a = g_i = 0$ . We will argue, however, that the amplitude of the  $h$

modes is small,  $\langle\langle h^2 \rangle\rangle \propto 1/\Omega$ , and thus it should only give a contribution to the measurement described in Sec. III B comparable with the statistical noise.

We first note that the staggered momentum density can appear in the equations for the momentum density and the number density only in even powers. To understand what is the mechanism that controls the growth of the staggered momentum density we will abstract from unnecessary details and consider a simplified problem which, however, contains all the essential ingredients.

Let us consider two boxes that can accommodate  $M$  objects each and let  $N_i$  be the number of objects in box  $i$ ,  $i = 1, 2$ . We can define  $H = N_1 - N_2$  and  $G = N_1 + N_2$ .

We now start throwing objects in the boxes. The probability that the next object will land in box  $i$ ,  $p_i$ , is

$$p_i = \frac{M - N_i}{2M - (N_1 + N_2)} \approx \frac{1}{2} - \frac{N_i - N_{j \neq i}}{4M} + O((N/M)^2) ,$$

where we are assuming that  $N_i/M \ll 1$ ,  $i = 1, 2$ . The resulting time evolution for  $H$  is then well approximated by

$$H(t+1) - H(t) = -\frac{1}{4M} H(t) + f(t) ,$$

with  $f(t)$  a random variable that can have the values  $\pm 1$  with equal probability; it is uncorrelated to  $H$  at prior times, and such that  $\langle\langle f(t_1)f(t_2) \rangle\rangle = \delta_{t_1,t_2}$ . It is then easy to compute

$$\langle\langle H^2 \rangle\rangle = \frac{2M}{1 - 1/8M} ;$$

thus  $\langle\langle (H/M)^2 \rangle\rangle \approx 2/M$ .

The parallels between this example and our problem are easily drawn: the two boxes represent, for a given staggered momentum density, say  $h_2$ , the lattice sites for which the phase factor  $e^{i\pi B_a \cdot r}$ , is respectively, equal to  $\pm 1$ ; the "object" is one unit of momentum along the  $x$  direction;  $G$  is the total momentum on the two sublattices; while  $H$  is the equivalent of the staggered momentum. An argument similar to the one described above applies to the staggered momentum density in our simulations, and it thus predicts that there should be a correction to the measured kinematic viscosity of the order of  $\langle\langle h_i^2 \rangle\rangle = C_0/\Omega$ , with  $C_0$  smaller than 1. In this model we do not give any mechanism to keep  $(N_1 + N_2)/M \ll 1$  but in the actual simulations this is provided by the momentum dissipation. This prediction has been checked numerically using a recently developed Boltzmann-equation technique (Ref. 40).

\*Present address: Program in Applied and Computational Mathematics, Princeton University, Princeton, NJ 08544.

<sup>1</sup>U. Frisch, B. Hasslacher, and Y. Pomeau, Phys. Rev. Lett. **56**, 1505 (1986).

<sup>2</sup>D. d'Humières, P. Lallemand, and U. Frisch, Europhys. Lett. **2**, 297 (1986).

<sup>3</sup>D. d'Humières, P. Lallemand, and G. Searby, in Proceedings of the Workshop on Large Nonlinear Systems [Complex Syst. **1**,

- 4 (1987)].
- <sup>4</sup>C. Burges and S. Zaleski, *Complex Syst.* **1**, 31 (1987).
- <sup>5</sup>See the bibliography of Ref. 3.
- <sup>6</sup>D. H. Rothman, *Geophysics* **53**, 509 (1988).
- <sup>7</sup>S. Wolfram, *J. Stat. Phys.* **45**, 471 (1986).
- <sup>8</sup>U. Frisch *et al.*, in Ref. 3.
- <sup>9</sup>Guy R. McNamara and Gianluigi Zanetti (unpublished).
- <sup>10</sup>G. Zanetti, *Phys. Rev. A* **40**, 1539 (1989).
- <sup>11</sup>D. d'Humières, P. Lallemand, and T. Shimomura (unpublished).
- <sup>12</sup>D. d'Humières and P. Lallemand, *C. R. Acad. Sci. Ser. I* **302**, 983 (1986).
- <sup>13</sup>L. P. Kadanoff, G. R. McNamara, and G. Zanetti, in Ref. 3.
- <sup>14</sup>K. Balasubramanian, F. Hayot, and W. F. Saam, *Phys. Rev. A* **36**, 2248 (1987).
- <sup>15</sup>B. Alder and T. Wainwright, *Phys. Rev. Lett.* **18**, 968 (1970).
- <sup>16</sup>J. R. Dorfman and E. G. D. Cohen, *Phys. Rev. Lett.* **25**, 1257 (1970).
- <sup>17</sup>D. Forster, D. Nelson, and M. Stephen, *Phys. Rev. A* **16**, 732 (1977).
- <sup>18</sup>N. Margolus, T. Toffoli, and G. Vichniac, *Phys. Rev. Lett.* **56**, 1694 (1986).
- <sup>19</sup>L. Hannon, G. C. Lie, and E. Clementi, *Phys. Lett. A* **119**, 174 (1986).
- <sup>20</sup>K. Kawasaki and J. D. Gunton, *Phys. Rev. A* **8**, 2048 (1973).
- <sup>21</sup>D. J. Evans and G. P. Morriss, *Phys. Rev. Lett.* **51**, 1776 (1983).
- <sup>22</sup>D. d'Humières and P. Lallemand, in Ref. 3.
- <sup>23</sup>J. P. Rivet, in Ref. 3.
- <sup>24</sup>M. Fixman, in *Advances in Chemical Physics*, edited by I. Prigogine (Interscience, New York, 1963), Vol. VI.
- <sup>25</sup>Y. Pomeau and P. Résibois, *Phys. Rep.* **19**, 63 (1975).
- <sup>26</sup>S. S. Orszag and V. Yakhot, *Phys. Rev. Lett.* **56**, 1691 (1986).
- <sup>27</sup>D. d'Humières and P. Lallemand, *Physica* **140A**, 327 (1986).
- <sup>28</sup>In the exchange particle  $\rightarrow$  holes [i.e.,  $d \rightarrow (1-d)$ ]  $\bar{g} \rightarrow -\bar{g}$  and variations in the number density  $\delta\bar{n}$  change sign. It is also easy to see that in the Taylor-series expansion of the equilibrium stress tensor all the coefficients of odd powers of  $\bar{g}$  are identically zero. Equation (2) at  $d = \frac{1}{2}$  should be completely symmetric with respect to the exchange  $d \rightarrow (1-d)$ ; hence for this value of  $d$  (assuming that the Taylor-series expansion is meaningful), Eq. (2) becomes linear in  $\bar{g}$ .
- <sup>29</sup>The actual forcing scheme is slightly more complicated since it must compensate for inhomogeneity in the momentum and number densities due to the macroscopic flow (see Sec. III). The forcing algorithm randomly selects a lattice row and column and then searches along the row until it finds a site where a forcing rule may be successfully applied. The program terminates if no forcing operation can be performed on a selected row. This guarantees that forcing operations will be uniformly distributed across the width of the channel, despite variations in the mass and momentum densities.
- <sup>30</sup>L. D. Meshalkin and Ya. G. Sinai, *J. Appl. Math.* **25**, 1700 (1961).
- <sup>31</sup>G. I. Sivashinsky, *Physica* **17D**, 243 (1985).
- <sup>32</sup>Z. S. She, in *Current Trends in Turbulent Research*, edited by Herman Branover, Michael Mond, and Yeshajahu Unger (AIAA, Providence, RI, 1988).
- <sup>33</sup>C. Cercignani, *Theory and Application of the Boltzmann Equation* (Elsevier, New York, 1975).
- <sup>34</sup>The mean free path can be easily computed from the collision rules of Fig. 2 and the resulting expression is in perfect agreement with the results of direct simulation.
- <sup>35</sup>J. Dahlburg, D. Montgomery, and G. Doolen, *Phys. Rev. A* **303**, 2471 (1987).
- <sup>36</sup>L. P. Kadanoff and J. Swift, *Phys. Rev.* **166**, 89 (1968).
- <sup>37</sup>L. Landau and E. Lifshitz, *Fluid Mechanics* (Pergamon, New York, 1986).
- <sup>38</sup>U. Frisch and J. P. Rivet, *C. R. Acad. Sci. Ser. I* **303**, 1065 (1986).
- <sup>39</sup>M. Hénon, in *Proceedings of the Modern Approaches to Large Nonlinear System Workshop*, Ref. 3.
- <sup>40</sup>F. J. Higuera and S. Succi, *Europhys. Lett.* **8**, 517 (1989); G. R. McNamara and G. Zanetti, *Phys. Rev. Lett.* **61**, 2332 (1988).
- <sup>41</sup>This is not in conflict with the result of Refs. 25 and 17 that predicts, for an incompressible 2D fluid, the law  $\nu(L) = \nu_0[1 + A \ln(L)]^{1/2}$ . Ours, as explained before, is a linearization of an equivalent formula around the value of the bare transport coefficients. At any rate the range of  $L$  accessible to our simulations does not allow us to discern between a linear dependence of  $\nu$  in  $\ln(L)$  or the above formula.
- <sup>42</sup>J. P. Rivet and U. Frisch, *C. R. Acad. Sci. Ser. I* **302**, 267 (1986).
- <sup>43</sup>From Eq. (A11) it appears that we are assuming the multi-transport modes to be orthogonal. While it is true that the scalar products  $\langle a, a'; q, q' | a''; q'' \rangle = \langle a, a'; a''; q, q' | a''', a''''; q''', q'''' \rangle = O(1/N)$ , the three coupled modes vector has a finite projection on  $|a; q\rangle$ . At any rate, this is irrelevant in writing Eq. (A11) since  $\langle \hat{\Pi}_{xy}(0) | a; q \rangle = 0$ .
- <sup>44</sup>The other possible vertices  $+-$ ,  $-+$ , and  $\pm 1$  give a negligible correction to the slope, Eq. (16), of second order in the prefactor of  $(2/\nu_{ce} + 1/\Gamma_{ce})$  in Eq. (16).
- <sup>45</sup>The calculation is analogous to the one shown in Ref. 31 for the forcing  $\mathbf{f} = (\sin(2\pi y), 0)$ , "Kolmogorov flow."
- <sup>46</sup>In principle, only sites that are at distance of one mean free path  $l$  can be considered uncorrelated. On the other hand, these equal-time correlation effects seem to be extremely weak; thus Eq. (C5) is a very good estimate.
- <sup>47</sup>Proceedings of the Workshop on Large Nonlinear Systems [*Complex Syst.* **1**, 4 (1987)].